Research Square

Preprints are preliminary reports that have not undergone peer review.
They should not be considered conclusive, used to inform clinical practice,
or referenced by the media as validated information.

Instability characteristics and stress-oriented fracturing mechanism of composite thick-hard roof in shallow stope

Xiaowu Zhang

zhxw667@llu.edu.cn

Lyuliang university

Yue Cao

China University of Mining and Technology

Weiyong Lu

Lyuliang university

Yaohui Sun

Lyuliang university

Lei Shi

Lyuliang university

Zhijun Xu

China University of Mining and Technology

Lianhai Tai

Anhui University of Science and Technology

Research Article

Keywords: Composite thick-hard roof, Rock pressure impact, stress-oriented fracturing, Strength weakening, Energy release

Posted Date: May 13th, 2026

DOI: https://doi.org/10.21203/rs.3.rs-9357149/v1

License: This work is licensed under a Creative Commons Attribution 4.0 International License.
Read Full License

Additional Declarations: No competing interests reported.

Instability characteristics and stress-oriented fracturing mechanism of composite thick-hard roof in shallow stope

Xiaowu Zhang[a], Yue Cao[b,c], Weiyong Lu[a], Yaohui Sun[a], Lei Shi[a], Zhijun Xu[b,c], Lianhai Tai[d]

(1. Department of Resource and Mechanical Engineering, Lyuliang University, Lvliang 033001, China ; 2. School of Mines, China University of Mining and Technology, Xuzhou 221116, China; 3. State Key Laboratory of Coal Resources and Safe Mining, China University of Mining and Technology, Xuzhou 221116, China;d. School of Mining Engineering, Anhui University of Science and Technology, Huainan 232001, China)

*Corresponding author: Zhang Xiaowu, Department of Resource and Mechanical Engineering, Lyuliang University, No. 1, Xueyuan Road, Lishi District, Lvliang City, 033001, Shanxi Province, China.

E-mail address: zhxw667@llu.edu.cn

Abstract: Composite thick-hard roof(CTHR) is characterized by substantial thickness, high mechanical strength, excellent load-bearing capacity, and remarkable elastic energy storage potential. Its sudden collapse tends to induce rock bursts due to the abrupt release of accumulated elastic energy. This study analyzes the layered bearing characteristics of the CTHR and reveals its stress-oriented fracturing mechanism. The bearing strength of the CTHR decreases significantly with the increase of the hanging roof length and the number of layered strata. After the implementation of stress-induced fracturing treatment, the CTHR is fragmented into small-sized rock blocks, and the "three-zone" structure of the overlying strata is clearly formed. Meanwhile, the total energy released by microseismic events is reduced by 36.98% compared with that before. The average periodic weighting interval is shortened from 35.24 m to 16.57 m, representing a reduction of 52.98%, and the peak weighting pressure is reduced from 8179.58 kN to 5618.49 kN, a decrease of 31.32%. The bearing strength of the CTHR has been effectively reduced, and the hazard of ground pressure impact has been significantly mitigated.

Key words: Composite thick-hard roof; Rock pressure impact; stress-oriented fracturing; Strength weakening; Energy release.

1. Introduction

As global energy demand continues to expand, the safe and efficient exploitation of coal resources remains crucial for industrial development[1,2]. Statistical data indicates that more than 65% of mining areas in China are affected by composite thick-hard roof(CTHR)[3-5]. Characterized by large thickness, high mechanical strength, and massive integrity, the CTHR are prone to forming extensive roof suspensions. This leads to abnormally high support stress at the working face, posing a severe threat to mine safety[6-8]. Furthermore, the sudden release of accumulated strain energy accompanying the sudden collapse of CTHR during mining operations frequently triggers shock-induced damage and rock bursts[9-11]. Therefore, artificial intervention to control the caving characteristics of CTHR, eliminate large-scale roof suspensions, and reduce the dynamic energy released during strata collapse is of paramount importance[12-14].

To mitigate these hazards, hydraulic fracturing has emerged as a highly effective pre-conditioning method. By utilizing high-pressure water to initiate and propagate fracture networks within the rock mass, this technique significantly weakens the hard roof[15-17]. In recent years, scholars have extensively applied hydraulic fracturing across various aspects of coal mining, including enhancing coal seam permeability, relieving face-end pressure, and pre-splitting hard roof[18-20]. Field applications and micro-seismic monitoring have demonstrated the efficacy of this approach[21,22]. For instance, hydraulic fracturing of hard roof has been

shown to reduce high-energy micro-seismic events (above 10^3 J) by 40%[23-26]. Other studies have confirmed that hydraulic fracturing promotes the caving of thick roofs[27-28], significantly reduces the advanced support stress[29,30], decreases the weighting step distance of the working face[31-33], and effectively prevents large-scale roof falls[34,36].

More importantly, common hydraulic fracturing designs fail to account for the dynamic influence of mining-induced stress fields on the propagation of hydraulic fractures[37-39]. Consequently, it is difficult to determine the optimal fracturing locations or accurately predict the trajectory and coverage of the fracture networks. Furthermore, common hydraulic fracturing operations are generally executed via inclined boreholes drilled into the roof[40-42]. This geometric constraint severely limits the effective length of the borehole within the target stratum, making it nearly impossible to achieve large-scale fracturing of the CTHR.

This paper establishes a theoretical model for the stress-oriented fracturing of composite thick-hard roof(CTHR) and analyzes the mining-induced stress concentration characteristics across its different layers. A physical scale model was constructed to simulate the stress-oriented fracturing and subsequent instability of the CTHR. Through physical similarity simulation, the energy release characteristics of the CTHR before and after stress-oriented fracturing are comparatively analyzed, elucidating the underlying mechanism of stress-oriented fracturing. Field monitoring results demonstrate that stress-oriented fracturing effectively shortens the breaking span of the CTHR, reduces the periodic weighting intensity at the working face, and ultimately eliminates the threat of rockbursts in the stope.

2. Stress-oriented fracturing principle of CTHR

2.1 Engineering background

The experimental stope investigated in this study is the 130206 working face of Yangchangwan Coal Mine, located in Yinchuan City, Ningxia Hui Autonomous Region, China. The experimental stope exhibits a north–south extent of approximately 26.15 km, an east–west width of around 19.48 km, and a total area of about 421.59 km². The average vertical burial depth of the stope is 237.4 m, with a continuous mining advance distance of 1648 m and a strike mining length of 200 m, as shown in Fig. 1. The working face is extracted by using the fully mechanized top-coal caving method.

The coal seam thickness varies from 8.2 m to 9.4 m, with an average thickness of 8.8 m, and the seam dip angle ranges from 3° to 9°, averaging 4°. A composite thick-hard roof(CTHR) exists above the coal seam, among which the upper composite thick-hard roof(CTHR) has a thickness of 52.4 m and the lower composite thick-hard roof(CTHR) is 18.10 m thick. Rock samples were obtained through in-situ drilling and subsequently prepared into standard specimens for laboratory testing. The resulting physico-mechanical parameters of the top-bottom strata are shown in Table 1.

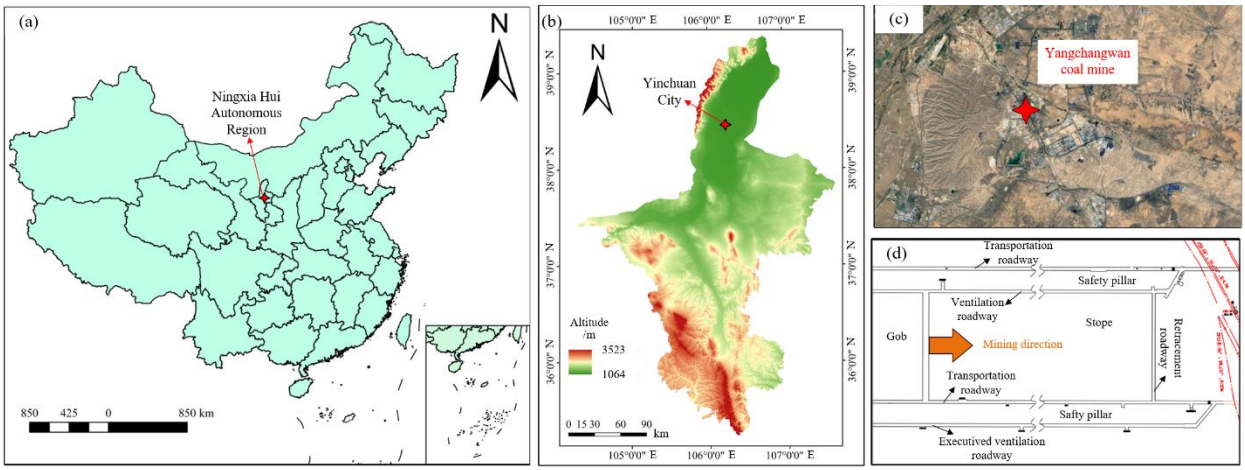


Fig. 1 Engineering background: (a) Geographical location; (b) Mine position; (c) Surface conditions; (d) Stope situation

Table 1 Characteristics and mechanical parameters of top-bottom strata

Lithology	Lithological description	Thickness /m	Density /kg·m^{-3}	UCS /MPa	Cohesive /MPa	Friction angle /°	Tensile strength /MPa
Sandy mudstone	Black; Muddy structure; Little of mica; Carbonized plant fossils.	33.30	2198	21.80	1.4	43	2.3
Silt sandstone	Light gray, Silty structure, horizontal bedding, Lots of coal chips.	3.80	2510	53.93	2.1	29	5.1
Medium sandstone	Gray white, Medium grained structure, Quartz, Argillaceous cementation.	4.10	2586	63.46	1.9	24	5.6
Silt sandstone	Light gray, Silty structure, horizontal bedding, Lots of coal chips.	6.30	2510	53.93	2.1	29	5.1
Coarse sandstone	Gray; Coarse grained structure; Mainly quartz; Argillaceous cementation.	52.40	2625	72.21	1.7	21	6.6
Medium sandstone	Gray white, Medium grained structure, Quartz, Argillaceous cementation.	18.10	2586	63.46	1.9	24	5.6
Sandy mudstone	Black; Muddy structure; Little of mica; Carbonized plant fossils.	2.00	2198	21.80	1.4	43	2.3
Coal	Black; Banded structure; Uneven fracture; Dark brown stripes.	8.80	1437	18.05	1.3	35	1.7
Sandy mudstone	Black; Muddy structure; Little of mica; Carbonized plant fossils.	14.90	2198	21.80	1.4	43	2.3

2.2 Stress-oriented fracturing principle of CTHR

In accordance with the fundamental criterion of rock mechanics, hydraulic fractures in rock masses always propagate perpendicular to the minimum principal stress and extend along the direction of the maximum principal stress[43-45]. Before the mining operation of the shallow stope, the vertical stress acting on the roof within the original stress zone—where the rock mass remains unaffected by mining activities—is lower than the horizontal stress. thus, horizontal hydraulic fractures are expected to form in this zone. As comparison, induced by mining, the stress state changes significantly, where the horizontal stress becomes the minimum principal stress and the vertical stress becomes the maximum principal stress, leading to the generation of vertical hydraulic fractures in this region.

Stress-oriented fracturing principle of the CTHR in shallow stopes: Firstly, horizontal hydraulic fractures are formed in the original stress zone of the roof through hydraulic fracturing, realizing the primary fracturing and weakening of the CTHR. With the coal extraction, the mining-induced stress field in the stope roof advances synchronously. When the stress concentration zone of the CTHR overlaps with the original stress zone, hydraulic fracturing in the stope roof will form vertical hydraulic fractures at this time, thereby achieving the secondary weakening of the CTHR, as shown in the Fig 2.

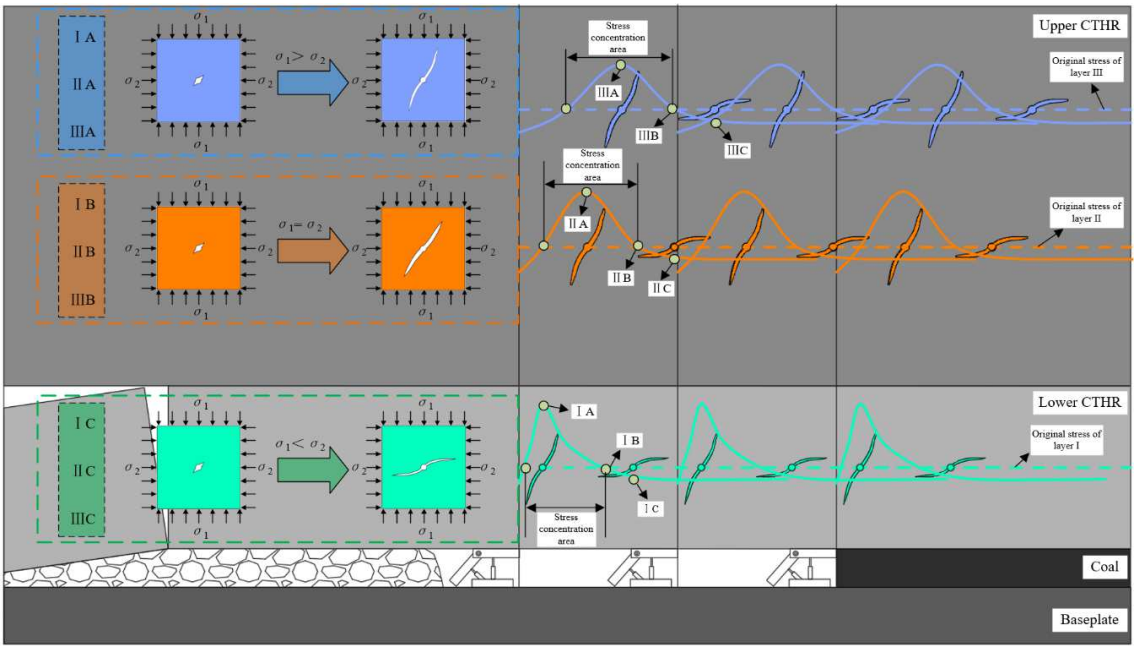


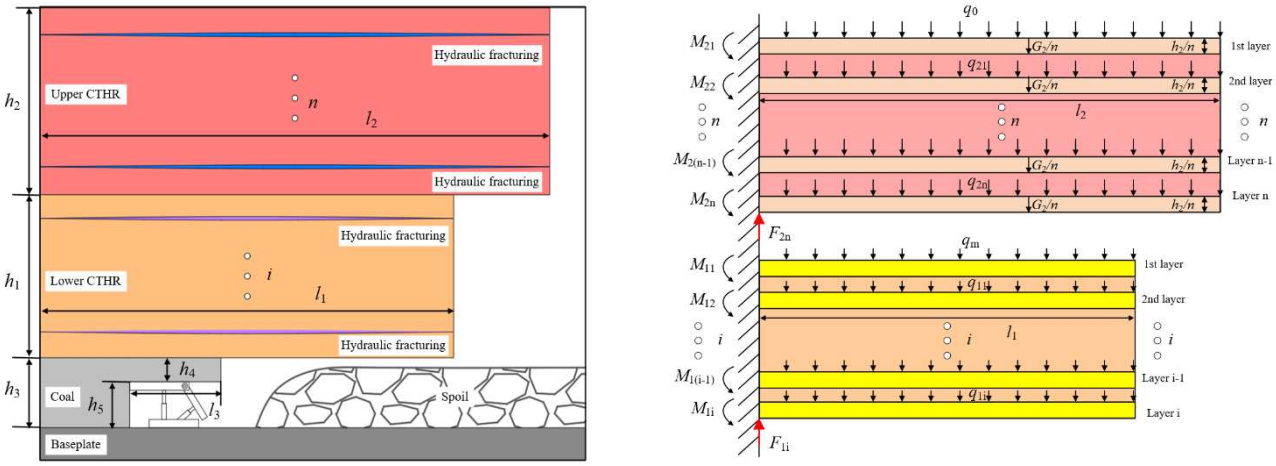
Fig 2 Stress-oriented fracturing principle of CTHR

3. Stress-oriented fracturing model of CTHR

3.1 Construction of mechanical model

After coal seam extraction, the unbroken CTHR adjacent to the working face exhibits a cantilever beam structure with one end fixed and the other free under the constraint of the surrounding rock mass. In this scenario, hydraulic fracturing is performed based on equal-thickness division, whereby the upper and lower CTHR are subdivided into n and i layers, respectively (Fig. 3).

In Fig. 3, h_1 and h_2 denote the thicknesses of the lower CTHR and upper CTHR, h_3 - h_5 denote the cutting height、caving height and coal height, respectively, while l_1 - l_3 represent the breaking spans of the lower and upper CTHR and the cantilever length of the top coal, respectively.



（a） Structural model （b） Mechanical model

Fig 3 Stress-oriented fracturing model of CTHR

3.2 Derivation of mechanical model

When the CTHR of the stope reaches its ultimate breaking state after stress-oriented fracturing, the overall load-bearing capacity of the rock strata satisfies the following equilibrium equation:

$$F_{1i} + F_{2n} - G_1 - G_2 - q_0 l_2 = 0 \quad (1)$$

$$\frac{G_1 l_1}{2}+\frac{q_0 {l_2}^2}{2}+\frac{G_2 l_2}{2}-\sum M_{1i}-\sum M_{2n}=0 \tag{2}$$

Specifically, the equilibrium condition for the ultimate load-bearing capacity of the lower CTHR is expressed as follows：

$$F_{1i}-q_{\mathrm{m}} l_1-G_1=0 \tag{3}$$

$$\frac{G_1 l_1}{2}+\frac{q_{\mathrm{m}} {l_1}^2}{2}-\sum M_{1i}=0 \tag{4}$$

In accordance with the superposed beam principle, intimate contact between the upper and lower CTHR is maintained throughout deformation, thereby ensuring that the bending moments of both strata satisfy Eq. (5).

$$\frac{\sum M_{1i}}{E_1 I_1}=\frac{\sum M_{2n}}{E_2 I_2} \tag{5}$$

Where: E_1 and E_2 are the elastic moduli of the lower CTHR and the upper CTHR, respectively(GPa); I_1 and I_2 represent the vertical section moments of inertia of the lower CTHR and the upper CTHR, respectively (m^4).

By solving the above equations simultaneously, the following expressions are obtained:

$$q_{\mathrm{m}}=\frac{-E_1 G_1 h_1 k l_1+E_1 h_1 l_2^2 q_0+E_1 G_2 h_1 l_2}{E_1 h_1 l_1^2+E_2 h_2 l_1^2} \tag{6}$$

$$F_{1i}=\frac{E_1 h_1 l_2^2 q_0+E_1 G_1 h_1 l_1+E_1 G_2 h_1 l_2}{E_1 h_1 l_1+E_2 h_2 l_1} \tag{7}$$

$$F_{2n}=\frac{E_1 h_1 k l_1 l_2 q_0+E_1 G_1 h_1 k l_1+E_1 G_2 h_1 k l_1+E_1 h_1 l_1 l_2 q_0-E_1 h_1 l_2^2 q_0+E_1 G_2 h_1 l_1-E_1 G_2 h_1 l_2}{E_1 h_1 l_1+E_2 h_2 l_1} \tag{8}$$

$$\sum M_{1i}=\frac{E_1 h_1 l_2^2 q_0+E_1 G_1 h_1 l_1+E_1 G_2 h_1 l_2}{2E_1 h_1+2E_2 h_2} \tag{9}$$

$$\sum M_{2n}=\frac{E_2 h_2 l_2^2 q_0+E_2 G_1 h_2 l_1+E_2 G_2 h_2 l_2}{2E_1 h_1+2E_2 h_2} \tag{10}$$

When the normal stress in the *i*-th sub-layer of the lower CTHR reaches the peak strength, the stratum fails, and:

$$\sigma_{1i}=\frac{\sum M_{1i}}{i W_{1i}} \le [\sigma_{1\max}] \tag{11}$$

Where: W_{1i} denotes the section modulus of resistance to bending of the *i*-th sub-layer of the lower CTHR; σ_{1i} represents the maximum normal stress in the i-th sub-layer of the lower CTHR, in megapascals (MPa).

Thus, the ultimate failure criterion of the lower CTHR is given by Eq. (12):

$$\sigma_{1i}=\frac{3E_1 h_1 i l_1^2 n\gamma_1+3E_1 h_2 i l_2^2 n\gamma_2+3E_1 i l_2^2 n q_0}{E_1 h_1 n+E_2 h_2 i} \le [\sigma_{1\max}] \tag{12}$$

The corresponding ultimate external load borne by the lower CTHR in the stope can then be expressed as Eq. (13).

$$q_{\text{low}} = \frac{-3E_1h_1il_1^2n\gamma_1 - 3E_1h_2il_2^2n\gamma_2 + E_1h_1n\sigma_1 + E_2h_2i\sigma_1}{3E_1il_2^2n} \tag{13}$$

Similarly, the fracture criterion for the n-th sub-layer of the upper CTHR is given by Eq. (14)

$$\sigma_{2n} = \frac{3E_2h_1il_1^2n\gamma_1 + 3E_2h_2il_2^2n\gamma_2 + 3E_2il_2^2nq_0}{E_1h_1n + E_2h_2i} \le [\sigma_{2\max}] \tag{14}$$

Where: $\sigma_{2\max}$ denotes the peak stress of the upper CTHR (MPa).

The corresponding ultimate external load of upper CTHR can be calculated using Eq. (15).

$$q_{\text{up}} = \frac{-3E_2h_1il_1^2n\gamma_1 - 3E_2h_2il_2^2n\gamma_2 + E_1h_1n\sigma_2 + E_2h_2i\sigma_2}{3E_2il_2^2n} \tag{15}$$

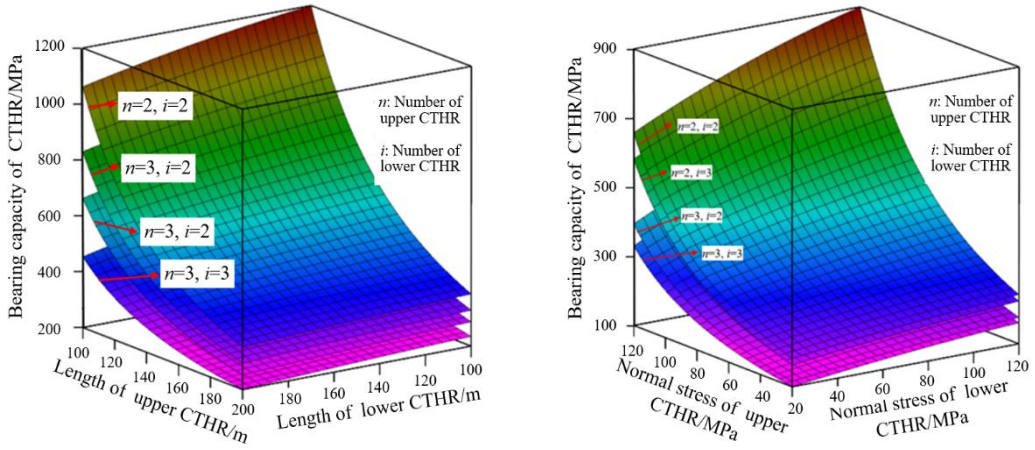
According to Eqs. (13) and (15), appropriate stress-oriented fracturing of the upper and lower CTHR enables their coordinated periodic failure at a reduced step span along the working face, thereby effectively mitigating strong strata pressure induced by CTHR failure within the stope.

3.3 Analysis of influencing factors

Based on the calculated stope conditions, the evolution of the bearing capacity of the CTHR after fracturing-induced weakening is obtained (Fig. 4). The ultimate bearing strength of the CTHR decreases significantly with increasing hanging length of both the upper and lower strata, with the upper CTHR exerting a more pronounced influence.

Similarly, a reduction in the maximum normal stress of the upper and lower CTHR leads to a marked decrease in the ultimate bearing strength, again with the upper CTHR having a greater effect. In addition, increasing the number of subdivided layers in both strata further reduces the overall bearing capacity, with layering of the upper CTHR contributing more significantly to the weakening effect.

Considering construction cost and operational feasibility, the optimal numbers of layers for the upper and lower CTHR are determined to be 3 and 2, respectively. Effective stratification of the CTHR through fracturing significantly reduces the overall bearing capacity of the roof, thereby mitigating long-distance hanging without collapse and improving the stress environment of the stope.



（a） Length of roof hanging （b） Maximum normal stress

Fig. 4 Bearing capacity evolution of CTHR

4.Evolution Characteristics of Mining-induced Stress Field in CTHR

4.1 Numerical Model Construction

Based on the occurrence characteristics of the rock strata at the experimental working face, a three-dimensional model with dimensions X × Y × Z=500 m × 500 m × 210 m was established (Fig. 5). Coal and rock were modeled using the Mohr-Coulomb constitutive model. Displacement constraints were applied at the bottom and lateral boundaries, and a uniformly distributed vertical load of 4 MPa was applied at the top to simulate the gravity of the overlying strata beyond the model, with a lateral pressure coefficient of 1.1. The model contains 5,062,500 elements and 5,166,082 nodes. The I, II, and III layers of the CTHR were defined at the mid-thickness of the 18.1 m medium-grained sandstone and at two-thirds of the thickness of the 62.8 m coarse-grained sandstone layers, corresponding to depths of 36.5 m, 68.6 m, and 89.6 m above the coal seam, respectively.

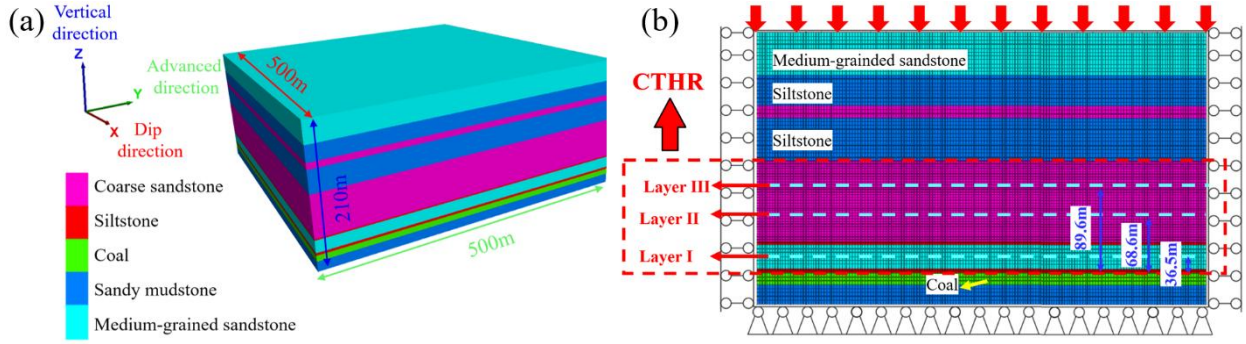
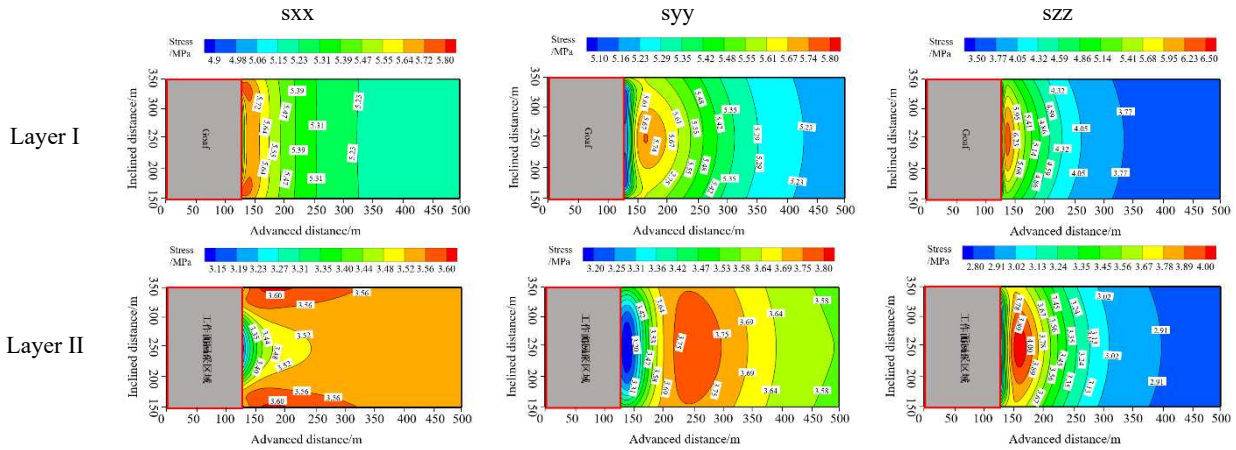


Fig. 5 Numerical model: (a) three-dimensional numerical model; (b) layering division of CTHR

4.2 Evolution law of mining-induced stress in CTHR

Fig. 6 shows stress contour maps of three-dimensional mining-induced stresses in the CTHR at different stages of stope advancement. Mining-induced stresses generally increase with the depth of the CTHR. As the working face advances, the dip, advance, and vertical stresses of the CTHR all rise, with both the advance and vertical stress fields exhibiting a stress concentration (“stress core”) effect.

When mining reaches 125 m, the stress field in the CTHR stabilizes, with the influence zone extending approximately 0 - 200 m ahead of the stope. Beyond this range, the effect of mining on the stress field can be neglected, indicating that the CTHR remain in the original stress zone. Moreover, continued advancement of the working face causes the direction of the minimum principal stress in the CTHR to shift from vertical to horizontal.



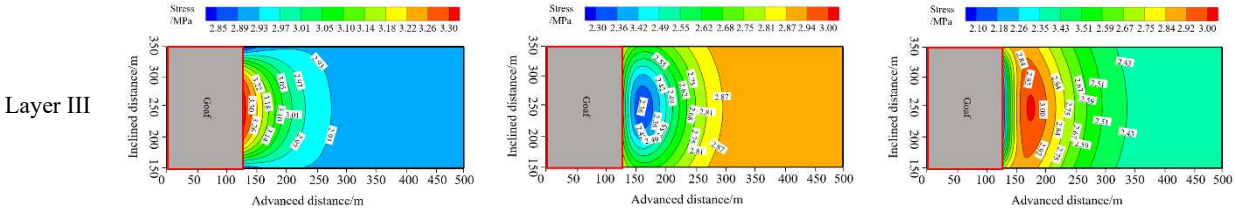


Fig. 6 Mining-induced stress at different layer of CTHR

4.3 Characteristics of mining-induced stress concentration in CTHR

Hydraulic fractures propagate perpendicular to the direction of the minimum principal stress [28–31]. To analyze the fracture propagation direction in different regions of the CTHR, the mining-induced stress fields of the I, II, and III layers were extracted. At each point in the CTHR, the directions and magnitudes of the maximum and minimum horizontal stresses were determined.

The ratios of the minimum vertical stress to the minimum horizontal stress and of the maximum horizontal stress to the minimum horizontal stress were defined as the stress concentration factors k_1 and k_2, respectively. These factors can be calculated using Eqs. (16) - (19).

$$s_{h\min} = \min(s_{sxx}, s_{syy}) \tag{16}$$

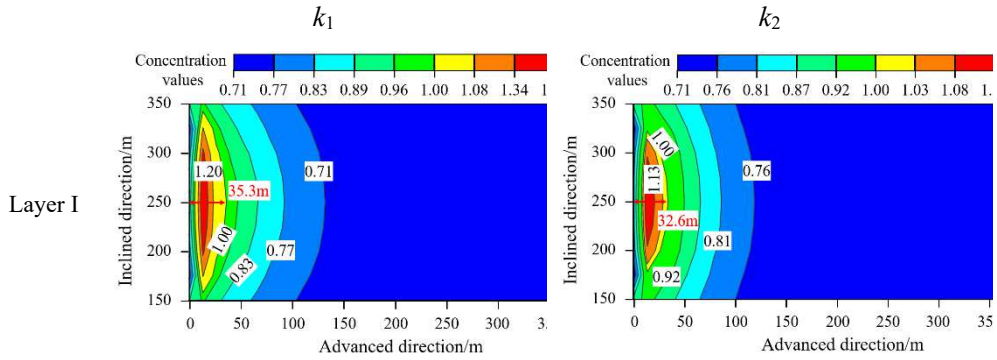
$$s_{h\max} = \max(s_{sxx}, s_{syy}) \tag{17}$$

$$k_1 = \frac{s_{szz}}{s_{h\min}} \tag{18}$$

$$k_2 = \frac{s_{szz}}{s_{h\max}} \tag{19}$$

In the equations, σ_{sxx}、σ_{syy} and σ_{szz} represent the dip, advance, and vertical stresses, respectively, while σ_{hmin} and σ_{hmax} denote the minimum and maximum horizontal stresses along the dip and advance directions, respectively.

Fig. 7 shows the contour maps of stress concentration factors in the CTHR. Along the stope direction, these factors increase and then decrease, forming a stress concentration "core." With increasing burial depth, the extent of the stress concentration zone gradually decreases. In the I, II, and III layers of the CTHR, the stress concentration zone extend approximately 10.3 - 32.6 m, 14.4 - 72.6 m, and 16.8 - 102.9 m ahead of the stope, respectively, whereas the original stress zones lie beyond 35.3 m, 84.3 m, and 124.7 m. Accordingly, hydraulic fracturing performed within the stress concentration zone at 20 m, 30 m, and 50 m in the I, II, and III layers, respectively, propagates vertically. In contrast, fracturing in the original stress zones at 200 m results in horizontal fracture propagation.



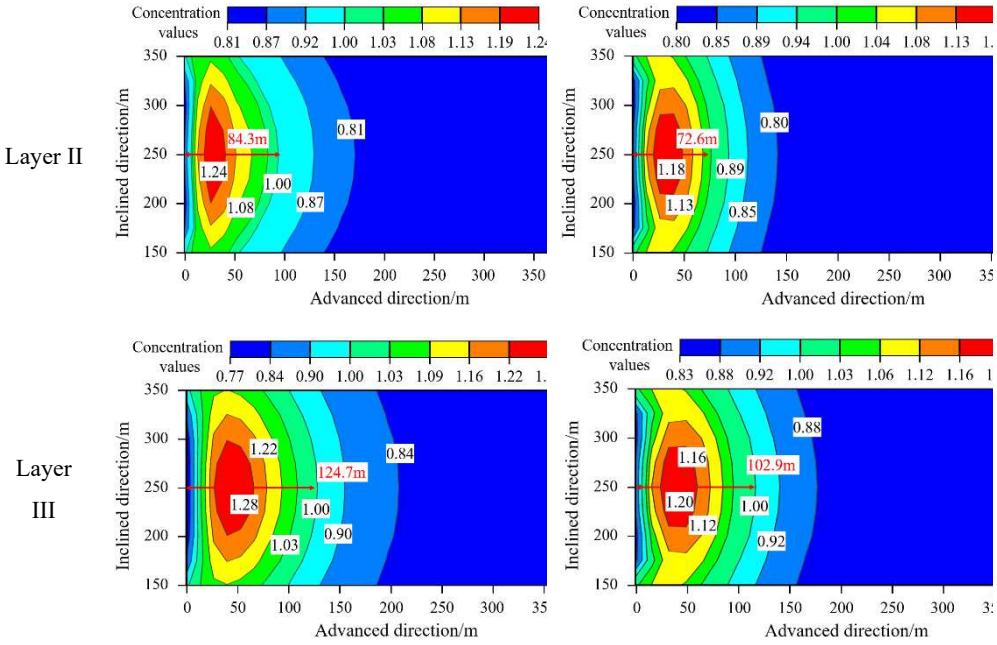


Fig 7 Stress concentration factor distribution in different layer of CTHR

5. Stress-oriented fracturing mechanism of CTHR

5.1 Model Construction

To analyze the fracture propagation behavior at different mining-induced stress concentration points in the CTHR, vertical stress σ_V and horizontal stress σ_H of the stope roof at 1.20, 1.10, 1.00, 0.90, and 0.80 were extracted. A numerical model with dimensions of 300 m × 300 m in length and width was then constructed (Fig. 8). The model was discretized into 22,500 solid elements, each measuring 0.5 m × 0.5 m.

The fracturing point was located at the geometric center of the model, with initial fractures of 1 m length set on either side. These fractures were inclined at 45° to the horizontal (X-axis) direction, and the fracturing process lasted 300 s. Fixed displacement constraints were applied along the model boundaries, and a hydrostatic pressure of 0 MPa was set as the initial boundary condition.

The model was defined as a linear elastic porous material, with physical and mechanical parameters listed in Table 2. The initial saturation of the model was set to 1.0, indicating that the pores were fully filled with fracturing fluid.

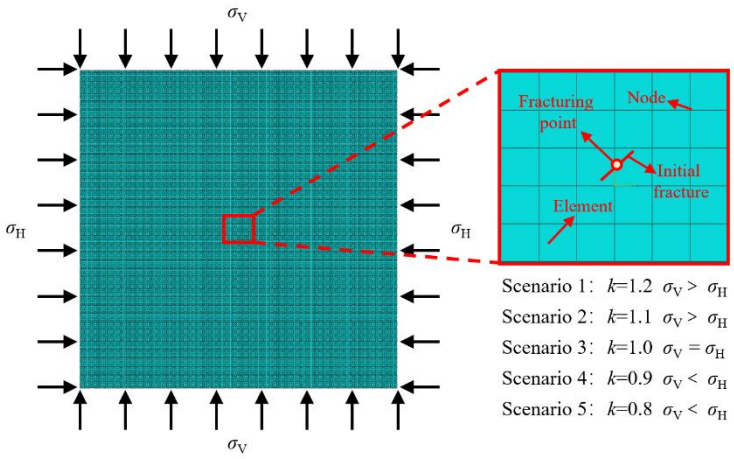


Fig 8 Numerical model

Table 2 Physical and mechanical parameters of model

Names	Elastic modulus /Pa	Tensile strength /Pa	Filtration coefficient	Fluid viscosity	Poisson's ratio	Permeability rate / $m \cdot s^{-1}$	Porosity ratio	Viscous regularization coefficient
Values	15×10^{9}	9.5×10^{6}	1.0×10^{-14}	0.001	0.25	1.0×10^{-7}	0.1	0.001

5.2 Propagation characteristics of stress-oriented fracture in CTHR

Fig. 9 illustrates the stress-oriented fracturing behavior of the CTHR. Although the initial fracture orientations are identical, the hydraulic fractures deviate significantly under different stress concentration factors due to the local stress field. In all cases, the final propagation direction remains perpendicular to the minimum principal stress, consistent with Refs. [31–33]. When the stress concentration factor equals 1.00, the hydraulic fracture propagates along the 45° initial fracture orientation. For stress concentration factors greater than 1.00, the fracture propagates vertically, whereas for factors less than 1.00, it propagates horizontally. The rate and magnitude of directional deviation increase with increasing stress concentration factor. Furthermore, a decrease in the stress concentration factor results in an increase in fracture width, as the stress threshold for fracture initiation and propagation is lower, facilitating hydraulic fracture development.

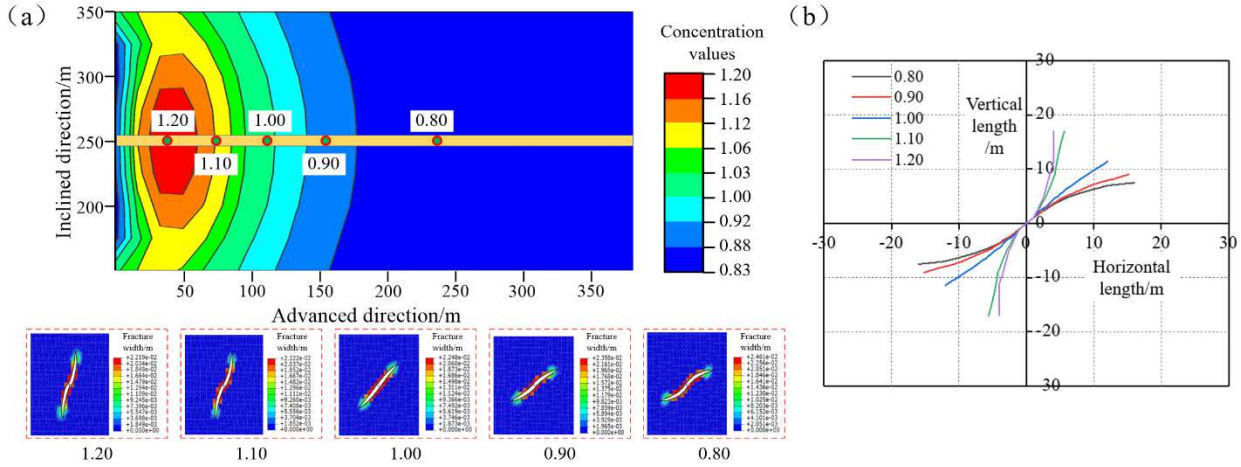


Fig 9 Stress-oriented fracturing characteristics of CTHR: (a) Fracture propagation morphology, (b) Crack propagation path

5.3 Variation of stress-oriented fracturing pressure

Fig. 10 illustrates the evolution of stress-oriented hydraulic fracturing pressure in the CTHR. Under different mining-induced stress concentration factors, the fracture propagation process follows a consistent pattern. Upon injection, part of the fracturing fluid is lost through filtration and seepage into the rock, increasing pore pressure, while the remaining fluid gradually fills the fracture, causing fluid pressure within the fracture to rise and the fracture to open.

When the fluid pressure reaches the rock's failure strength, new fractures are generated, and fluid enters these fractures, leading to a sudden drop in fracture pressure and a temporary halt in propagation. Continued fluid injection causes the pressure in the newly formed fracture to rise again, triggering further fracture propagation once the failure strength is exceeded. This cyclical process produces a sawtooth-shaped fluid pressure curve.

Furthermore, increasing the mining-induced stress concentration factor delays the initial fracturing time and raises the initiation pressure. This is attributed to the higher stress intensity in the rock, which increases the threshold stress required for fracture initiation and propagation.

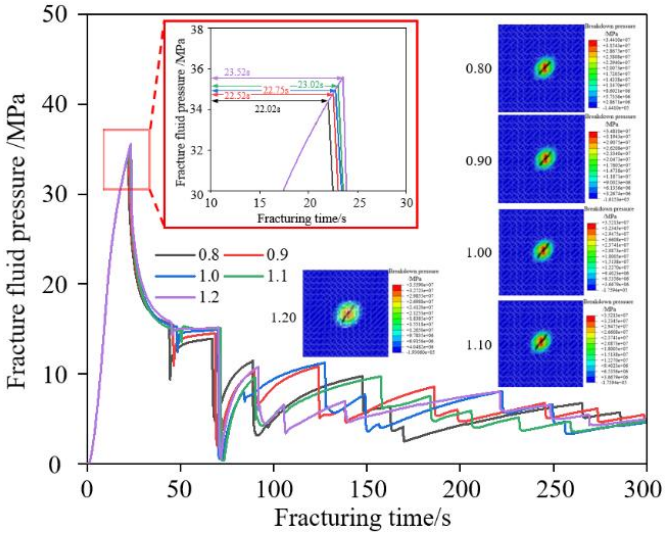


Fig 10 Evolution of stress-oriented fracturing pressure

6. Stress-oriented fracturing mechanism of CTHR

6.1 Physical Similar Simulation Test Scheme

（1）Model mixing ratio

Two test platforms, each measuring 2500 mm × 200 mm × 1500 mm (L × W × H), were used to construct a 2D physical similarity model. Based on the stope roof conditions and the similarity theory, the similarity ratios were determined as follows: unit weight similarity ratio 1.667, geometric similarity ratio 125, kinematic similarity ratio 11.18, and stress similarity ratio 208.4.

The model material was composed of sand as the aggregate, lime and gypsum as binders, and mica to simulate inter-layer separation. Eleven distinct coal and rock strata layers were reproduced, with detailed parameters listed in Table 3. The overburden gravitational load and in-situ lateral stress were applied pneumatically, corresponding to 10 kPa and 2 kPa, respectively.

Table 3 Mixing ratio parameters of similar model

No.	Lithology	Actual thickness /m	Simulated thickness /cm	Sand /kg	Lime /kg	Gypsum /kg
11	Sandy mudstone	23.35	18.68	220.16	25.69	11.01
10	Coarse sandstone	9.20	7.36	80.96	6.07	14.17
9	Sandy mudstone	33.30	26.64	313.97	36.63	15.70
8	Silt sandstone	3.80	3.04	33.44	4.18	4.18
7	Medium sandstone	4.10	3.28	33.83	5.64	5.64
6	Silt sandstone	6.30	5.04	55.44	6.93	6.93
5	Coarse sandstone	52.40	41.92	461.12	34.58	80.70
4	Medium sandstone	18.10	14.48	149.33	24.89	24.89
3	Sandy mudstone	2.00	1.60	18.86	2.20	0.94
2	Coal	8.80	7.04	84.70	8.47	3.63
1	Sandy mudstone	14.90	11.92	140.49	16.39	7.02

（2）Stress-oriented fracturing and excavation

To minimize boundary effects, 40 cm coal pillars were reserved at both the left and right sides of the model. Following the similarity theory, excavation was conducted from left to right, with a step length of 6.0 cm and an interval of 45 min. Excavation was terminated when the cumulative length reached 170 cm.

Ultra-thin, high-density EPS foam boards were pre-embedded in the roof to simulate hydraulic fractures

(HFs). In Layer I (10.21 cm above the coal seam), nine vertical and six horizontal HFs were evenly arranged at 25.14 cm intervals, located 77.63 cm and 136.98 cm from the left boundary, respectively. In Layer II (41.47 cm above the coal seam), eight vertical and six horizontal HFs were arranged at the same interval, located 94.17 cm and 151.74 cm from the left boundary. In Layer III (10.21 cm above the coal seam), seven vertical and five horizontal HFs were arranged at the same interval, located 112.41 cm and 170.12 cm from the left boundary. Before excavation, a specialized resistance hot melter was used to melt the foam boards, simulating the HFs. Excavation then proceeded according to the prescribed steps.

（3）Displacement Monitoring

Non-contact, full-field displacement measurements of overlying rock settlement were conducted using the VIC-3D system (CSI, USA). High-definition images were captured by binocular industrial cameras and analyzed using VIC-Snap software. By examining the evolution of overlying strata displacement, the mechanism of stress-oriented fracturing of the CTHR were assessed

（4）Microseismic Monitoring

The Portable Paladin 5 microseismic monitoring system (ESG Solutions, Canada) was employed to record the magnitude, frequency, and locations of energy release during overlying rock fracturing. Five microseismic sensors were installed in the model. Sensors 2 - 4 were positioned in the uppermost overlying strata, with sensors 2 and 4 located 18 cm from the left and right boundaries and 8 cm from the top of the model. Sensors 1 and 5 were placed in the lower CTHR, each 18 cm from the left and right boundaries and 10.21 cm above the coal seam (Fig. 11). Analysis of microseismic data during mining revealed the evolution of the energy field associated with overlying rock fracture.

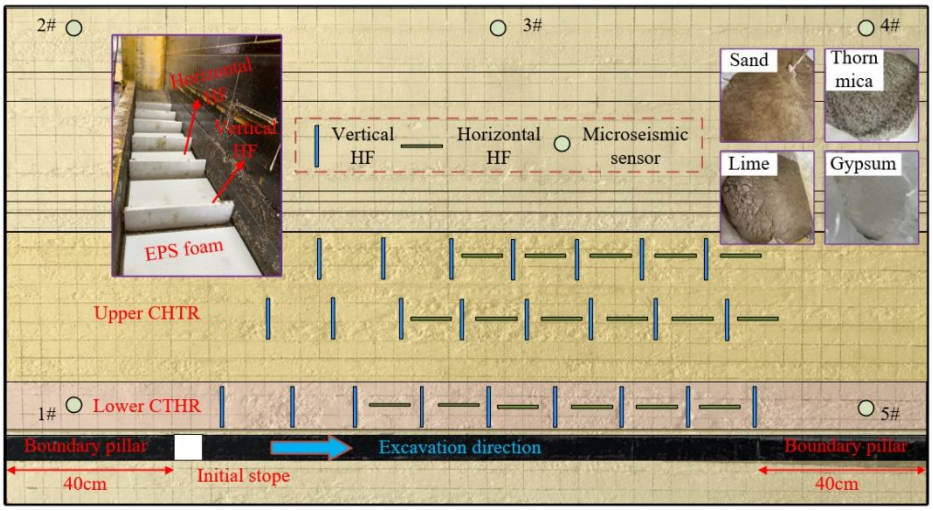


Fig. 11 Similar model and monitoring layout

6.2 Caving Characteristics of CTHR

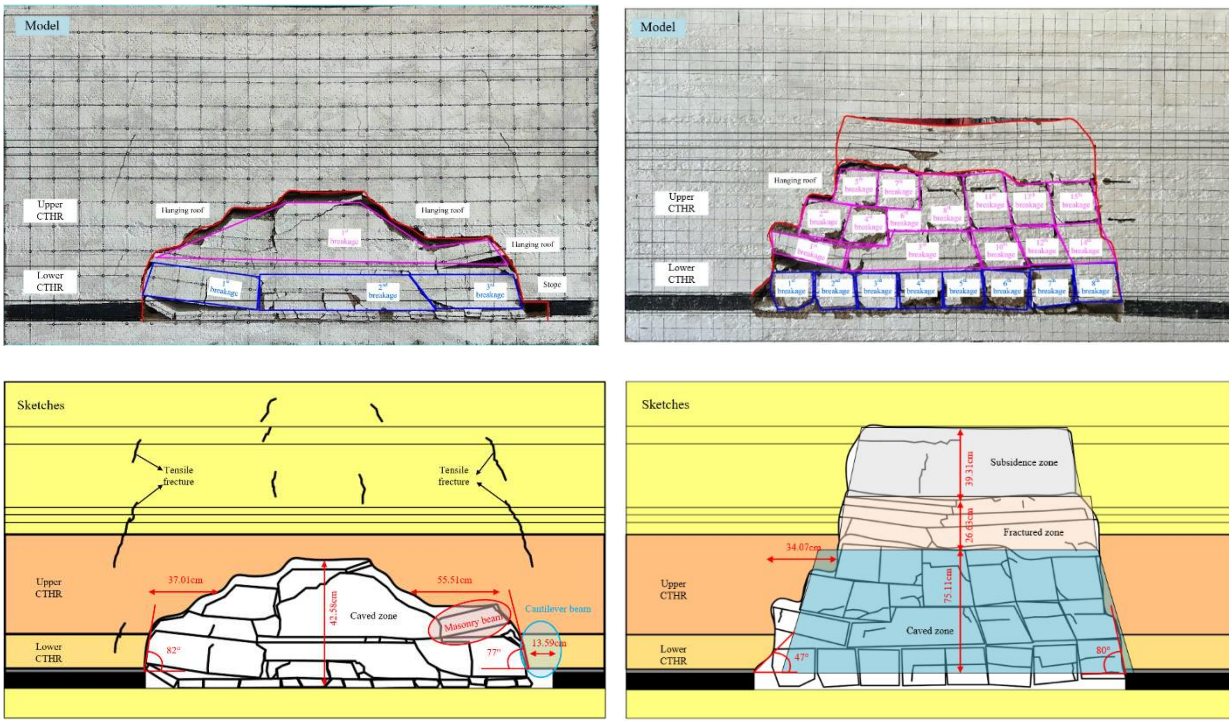
Significant differences exist in the overlying rock caving behavior during stope mining between pre- and post-fracturing models of the CTHR.

As shown in Fig. 12(a), in the absence of pre-fracturing, the immediate roof collapses almost instantaneously with the mining advance at the initial extraction stage. The fallen gangue fails to establish effective contact with the underlying CTHR. With continued mining, the lower CTHR forms a large-scale suspended roof structure following the collapse of the immediate roof. Upon reaching the critical span, the entire structural system undergoes catastrophic and unstable failure. The rock fragments generated by the fracture and collapse of the lower CTHR are relatively large, with average length and thickness of 46.78 cm and 13.29 cm, respectively, making the roof prone to severe support crushing incidents. When mining reaches the stop line, the upper CTHR fractures and caves suddenly, substantially enlarging the overlying rock collapse space. The

maximum caving height from the coal seam floor reaches 42.58 cm. At this stage, rotational instability of the upper CTHR, combined with synchronous catastrophic fracture of the lower CTHR, triggers intense rock burst phenomena in the working face. Furthermore, after CTHR collapse, residual cantilever beams persist above the working face, with cantilever lengths of 13.59 cm and 55.51 cm for the lower and upper CTHR, respectively. Consequently, the abutment pressure on the working face remains high, posing significant challenges to stope stability.

In contrast, Fig. 12(b) shows that after secondary fracturing and weakening of the CTHR, fractures develop progressively within the overlying strata. As the working face advances, these fractures penetrate the rock mass, preventing the formation of significant hanging roof structures. Roof collapse occurs in a timely manner, with average rock block length and thickness of 14.52 cm and 13.25 cm, respectively, providing effective self-supporting fill within the goaf. When mining reaches the stop line, the upper strata of the CTHR fracture and collapse, and the overlying rock undergoes overall bending and subsidence, forming a typical three-zone structure: caving zone height 75.11 cm, fractured zone height 26.63 cm, and bending subsidence zone height 39.31 cm.

Under the combined effects of mining disturbance and stress-oriented fracturing, the CTHR exhibits a higher damage height, while the dynamic force and energy released by fracturing are relatively small. This reduces both the weighting interval and intensity. Additionally, no cantilever beam is formed above the working face, resulting in a significant reduction of the abutment pressure.



（a） Before fracturing of CTHR （b） After fracturing of CTHR

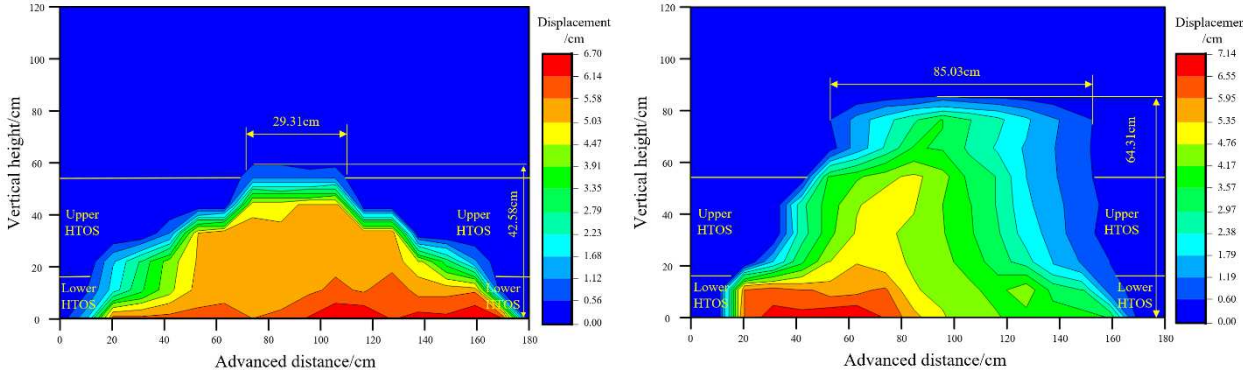
Fig. 12 Caving characteristics of CTHR

6.3 Settlement migration law of CTHR

Fig. 13 presents the cloud maps of overlying rock settlement and migration before and after stress-oriented fracturing of the CTHR in the stope. As shown in Fig. 13(a), before stress-oriented fracturing, the range of overlying rock affected by mining is relatively limited. The maximum settlement height reaches 42.58 cm, and the strike width of the top settled stratum is 29.31 cm. The overall displacement of the CTHR is large, with 87.53% of the rock stratum exhibiting displacement greater than 5.03 cm. Contour lines for displacements less than 4.47 cm are relatively dense. At this stage, no significant separation or fracturing occurs between rock

strata, indicating synchronous instability. The maximum settlement occurs far from the open-off cut, suggesting that roof hanging is pronounced in the initial mining stage. Continuous advancement leads to unstable fracturing of the rock stratum and a marked increase in roof displacement.

In contrast, Fig. 13(b) shows that after stress-oriented fracturing, the affected range of overlying rock expands substantially. The maximum settlement height reaches 64.31 cm, with a strike width of 85.03 cm at the top settled stratum. Displacement contours are more evenly distributed, and the mining process exhibits a clear "settlement–separation–fracture–instability" progression. The maximum displacement now occurs near the open-off cut, indicating timely collapse of the CTHR with mining advance, and periodic unstable fracture of the rock stratum as the working face progresses.



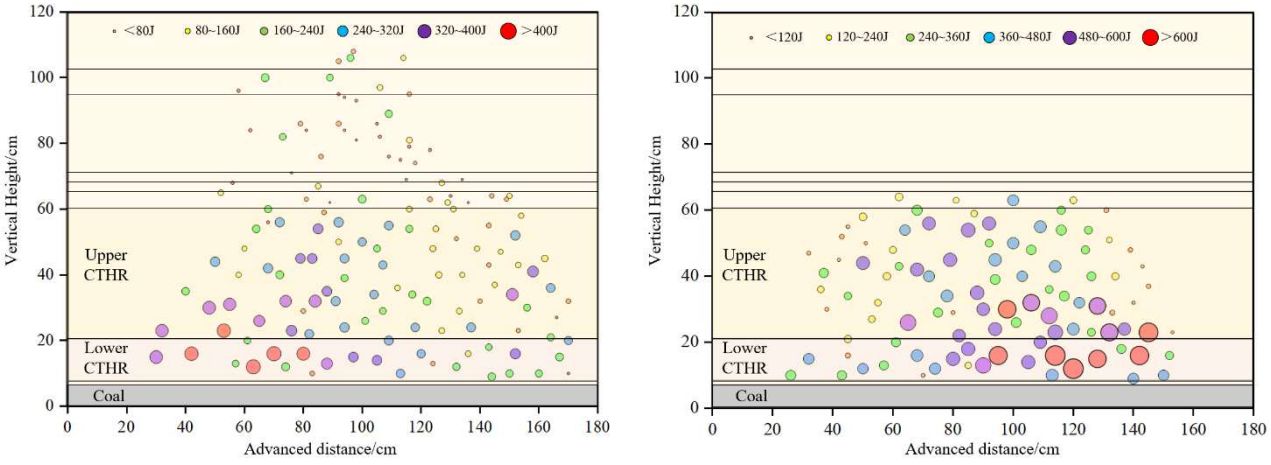
（a） Before fracturing of CTHR　　（b） After fracturing of CTHR

Fig. 13 Settlement migration law of CTHR

6.4 Energy evolution law of CTHR

Mining induces the initiation and propagation of numerous microcracks within the rock mass. When these cracks accumulate to a critical threshold, catastrophic rock failure occurs, accompanied by the release of elastic energy, which is manifested as microseismic events[46,47]. Fig. 14 presents the spatial and temporal distribution of microseismic energy before and after stress-oriented fracturing of the CTHR. Before secondary fracturing, microseismic events were primarily concentrated within the CTHR, characterized by high-energy and dense spatial distribution. A total of 103 microseismic events were recorded throughout the mining process, with an average energy magnitude of 358.09 J.

After stress-oriented fracturing of the CTHR, microseismic events became more uniformly distributed across the overlying strata, exhibiting lower energy and wider spatial coverage. Specifically, 147 microseismic events were recorded during mining, with the average energy magnitude reduced to 201.17 J, corresponding to a 43.82% decrease compared with the pre-fracturing stage. These results indicate that stress-oriented fracturing effectively mitigates the accumulation of elastic strain energy in the CTHR, while promoting more uniform energy dissipation during rock mass failure.



（a） Before fracturing of CTHR （b） After fracturing of CTHR

Fig. 14 Energy distribution characteristics of CTHR

Fig. 15 illustrates the evolution of microseismic energy in the roof strata at different mining stages. Before stress-oriented fracturing of the CTHR, three periodic weighting events were recorded. The first occurred at a mining advance of 82 cm, corresponding to fracture of the lower CTHR and a total microseismic energy of 11,891.38 J. The second event took place at 137 cm, during which the CTHR experienced combined fracture and instability, releasing 42,757.40 J of microseismic energy. The third event occurred at 180 cm, involving catastrophic fracture and instability of the CTHR, with a peak total microseismic energy of 52,808.71 J.

After stress-oriented fracturing, eight periodic weighting events were observed, with a cumulative microseismic energy of 33,278.47 J. This corresponds to a 36.98% reduction compared with the pre-fracturing condition. These results indicate that stress-oriented fracturing effectively reduces the elastic strain energy accumulated in the CTHR, suppressing the intensity of energy release during periodic weighting and mitigating the risk of intense rock burst events.

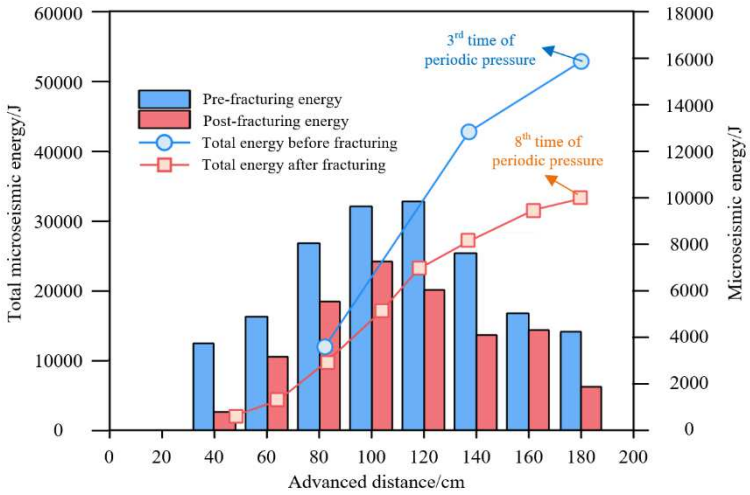


Fig. 15 Energy evolution law of CTHR

7. Field monitoring

7.1 Evolution law of fracturing pressure

A remote recording system was employed to monitor the fracturing pressure of the water pump unit in real time, allowing the dynamic evolution of the stress-oriented fracturing pressure of the CTHR to be captured, as shown in Fig. 16. During fracturing of rock strata at different horizons, the pressure initially rises rapidly due to the injection of high-pressure water. Once the fracturing pressure exceeds the rock strength, macroscopic cracks form, resulting in an abrupt pressure drop. This produces a serrated fluctuation in the pressure curve, while microcracks continue to propagate around the boreholes. Furthermore, the average fracturing pressure of the CTHR decreases with increasing fracturing horizon. Specifically, the initial fracturing pressures for layers I, II, and III of the CTHR are 53.53 MPa, 41.98 MPa, and 30.62 MPa, respectively, indicating that the deeper or higher layers require progressively lower pressures to initiate fracturing.

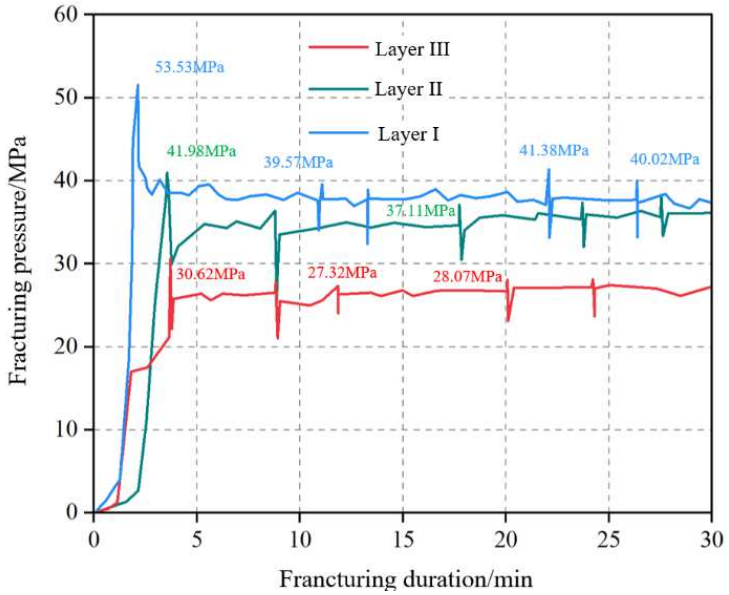
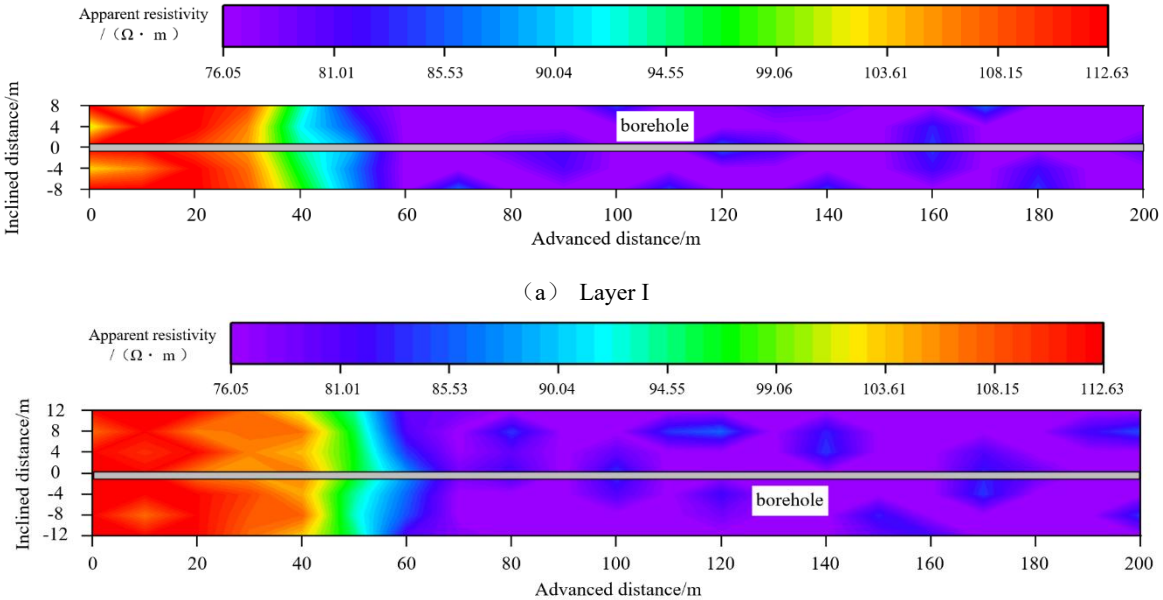


Fig. 16 Fracturing pressure evolution law during stress-oriented fracturing

7.2 Fracture propagation range monitoring

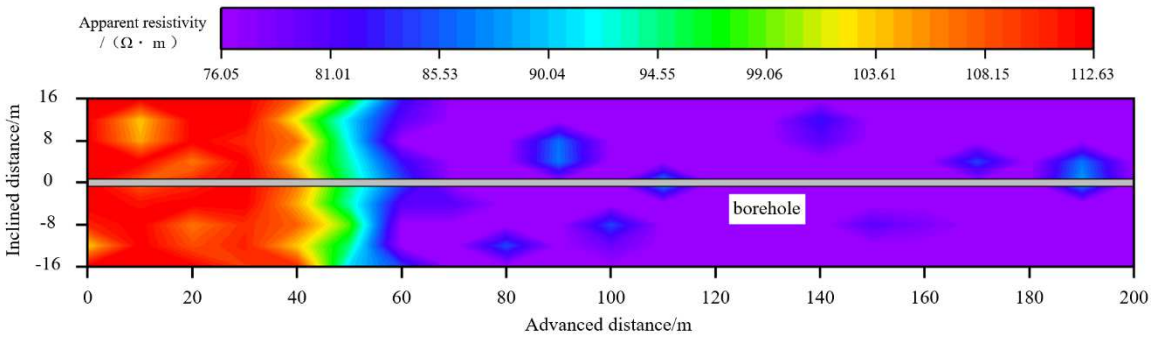
A YCS504 borehole transient electromagnetic detector was employed to characterize the fracture propagation range, and the corresponding apparent resistivity distribution was mapped, as shown in Fig. 17. During stress-oriented fracturing of the CTHR, hydraulic fractures propagated radially outward from the borehole, promoting secondary fracture development and interconnection within the rock mass. The radial propagation of fractures was ultimately constrained by seepage effects within the rock.

From the vertical cross-section of the borehole, the boundary of the apparent resistivity reduction zone in the fractured area was generally located at a radial distance of approximately 24 m from the borehole. Specifically, the fracture propagation ranges for layers I, II, and III were approximately 32 m, 24 m, and 16 m, respectively, indicating that the propagation extent decreases with increasing fracture horizon depth.



（a） Layer I

（b） Layer II

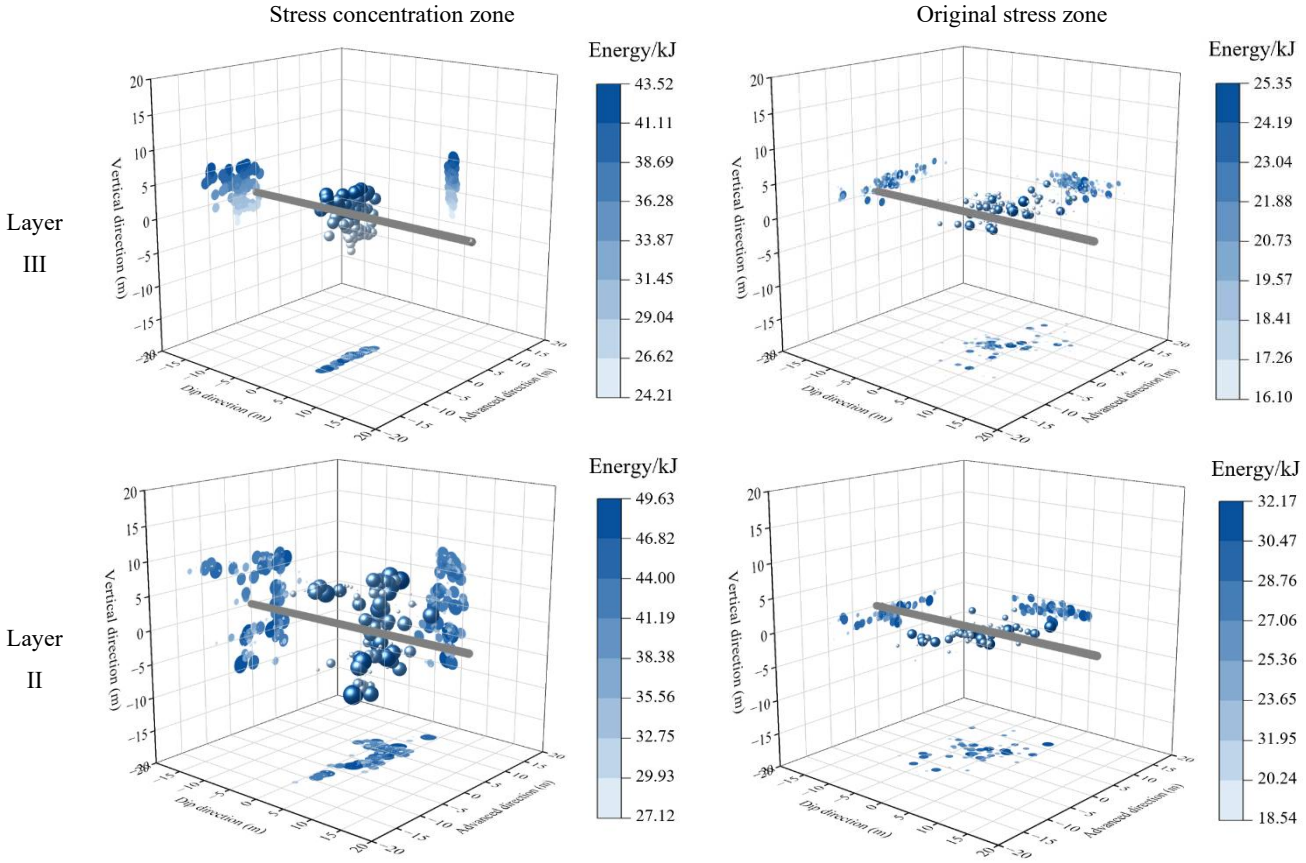


（c） Layer III

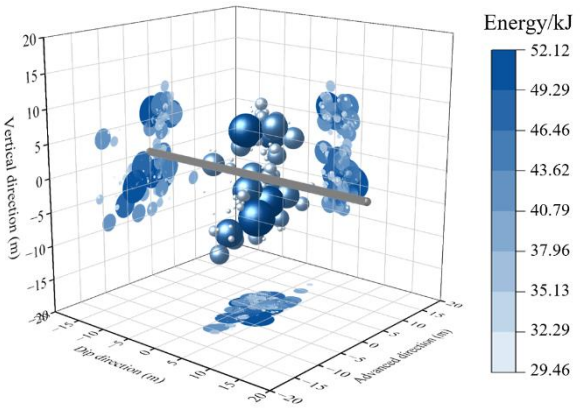
Fig. 17 Fracture propagation range of CTHR

7.3 Micro-seismic monitoring of fracture expansion

Fig. 18 illustrates the three-dimensional spatial distribution of microseismic events during stress-oriented fracturing of the CTHR. Along the advance direction of the stope, the energy of microseismic events within the stress concentration zones is significantly higher than that in the original stress zones at the same horizon. This is attributed to the greater mining-induced stress in the stress concentration zone, which requires higher energy for fracture propagation. Conversely, within the same roof area, higher CTHR layers exhibit lower microseismic energy during stress-oriented fracturing. This occurs because upper layers are subjected to a smaller overburden load, resulting in lower internal stress and reduced energy demand for fracture propagation. Furthermore, when stress-oriented fracturing is conducted in the stress concentration zones, microseismic events are primarily distributed in the vertical direction. In contrast, fracturing within the original stress zones produces microseismic events that are predominantly oriented horizontally.



Layer I



NA

Fig 18 Rose diagram of micro-seismic events in CTHR

7.4 Distribution characteristics of support resistance

Based on resistance data collected from stope supports, a cloud map illustrating the variation of support resistance with working face advancement was generated, as shown in Fig. 19. Before stress-oriented fracturing of the CTHR, the average periodic weighting step distance in the stope was 35.24 m, affecting 106 hydraulic supports. The pre-weighting peak load was 7,823.51 kN, while the peak load during weighting reached 8,179.58 kN, indicating a high intensity of periodic weighting.

After stress-oriented fracturing, the average periodic weighting step distance decreased to 16.57 m, involving 67 hydraulic supports. The pre-weighting peak load was 5,106.57 kN, and the peak load during weighting was 5,618.49 kN. Compared with the pre-fracturing condition, the average step distance was reduced by 52.98%, the pre-weighting peak load decreased by 34.73%, and the peak load during weighting decreased by 31.32%. These results demonstrate that stress-oriented fracturing of the CTHR effectively reduces the intensity of periodic weighting in the stope, thereby enhancing the safety of mining operations.

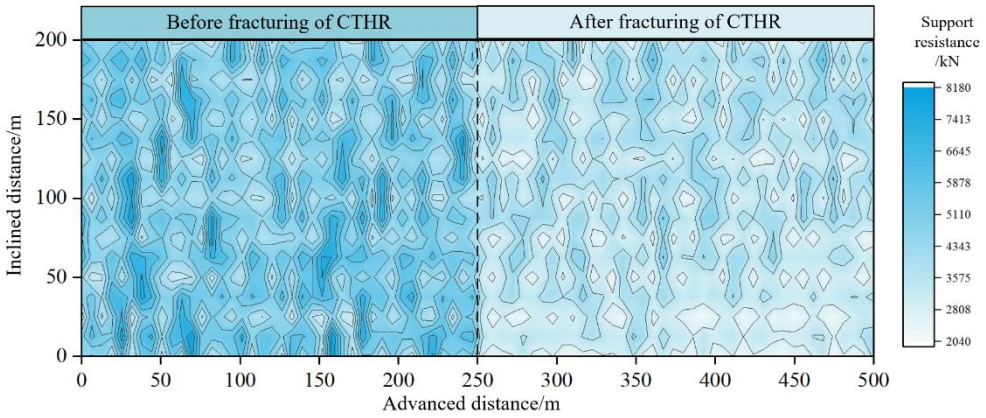


Fig. 19 Support resistance of CTHR

8.Conclusion

(1) The stress field within the composite thick-hard roof(CTHR)exhibits a step-like variation along the advance direction of the working face. When the working face advance exceeds 200 m, the three-dimensional stress field of the surrounding rock remains essentially unchanged, indicating that the CTHR are located within the original rock stress zone. In contrast, the CTHR in the advancing area are significantly influenced by the support stress, with vertical stress increasing noticeably and gradually surpassing horizontal stress. Stress concentration zones at different CTHR layers display a roughly circular distribution, with the stress concentration coefficient increasing toward the center and decreasing outward.

(2) Fracture propagation varies according to the local mining-induced stress distribution in the CTHR. Fractures in stress concentration zones predominantly propagate vertically, whereas those in the original stress zones propagate horizontally. In addition, the fracture propagation pressure in stress concentration zones is

substantially higher than in the original stress zones. Furthermore, the required fracture propagation pressure gradually decreases with increasing fracturing horizon.

(3) Before stress-oriented fracturing, the average energy released per microseismic event was 358.09 J, and three periodic weighting events occurred during the mining process, with a cumulative microseismic energy of 52,808.71 J; After stress-oriented fracturing of the CTHR, the average energy per event decreased to 201.17 J, representing a 43.82% reduction compared to the pre-fracturing condition. A total of eight periodic weighting events occurred during mining, with cumulative microseismic energy amounting to 33,278.47 J, corresponding to a 36.98% reduction relative to the pre-fracturing stage.

(4) By employing the stress-oriented fracturing mechanism, vertical and horizontal hydraulic fractures are formed in the stress concentration zone and original stress zone, respectively, achieving secondary weakening of the CTHR. Following stress-oriented fracturing, the support resistance at the working face is significantly reduced, the roof weighting step distance and peak strength are markedly decreased, and the frequency of weighting events is increased. These effects are conducive to improved management of mine pressure at the working face.

Conflicts of Interest

The authors declare no potential conflict of interest, and the manuscript is approved by all authors for publication.

Funding

This paper was supported by the Key projects of the Joint Fund of the National Natural Science Foundation of China(U21A20107), Key Research and Development of Lvliang City (2025GY20), Research Fund of State and Local Joint Engineering Laboratory for Gas Drainage & Ground Control of Deep Mines (Henan Polytechnic University) (SJF202503), the Fundamental Research Program of Shanxi Province (202303021222249) and the Key R&D Program for the Introduction of High - level Scientific and Technological Talents in Lüliang City (2023RC19),

References

[1] KANG HP，JIANG PF, YANG JW, et al. Theory and complete technology for collaborative control of surrounding rock in deep coal mine roadways. Journal of China Coal Society. 2026;51(1), 60−92.

[2] SUN SQ，ZHANG QiL，YANG F，et al. Research progress on regulation of hydraulic fracture propagation in coal seams. Coal Science and Technology.2026;54(1), 303−319.

[3] MA Y, WU QY, LI JZ, et al. Mechanism of weakening pressure arch of hydraulic fracturing to regulate mininginduced stresses. Journal of Mining and Strata Control Engineering, 2025; 7(4), 043542.

[4] LI ZZ, WANG R. Disaster mechanism of thick-hard roof and control technology by hydraulic fracture with directional long borehole. Coal Science and Technology. 2025,23(03), 103-106.

[5] HE ZQ, XIE HP, GAO MZ, et al. The fracturing models of hard roofs and spatiotemporal law of mining-induced stress in a top coal caving face with an extra-thick coal seam. Geomechanics and Geophysics for Geo-Energy and Geo-Resources. 2020;7(1), 465-488.

[6] LI Y, TAI Y, YU B, et al. Control of uniform surface settlement in coal mining: a pillarless coal mining method based on a chainsaw arm machine. Geomechanics and Geophysics for Geo-Energy and Geo-Resources. 2025;11(1), 118.

[7] GAO R, XU B, BAI D, et al. Influence of fracturing spacing on rock mass fracturing and energy evolution in overlying strata. Theoretical and Applied Fracture Mechanics. 2025;140, 105174.

[8] TAI Y, KUANG TJ, Yu B, et al. Hard Roof's 3D breaking characteristics for longwall faces mined via roof-cutting technology with a chainsaw arm machine. Rock Mechanics and Rock Engineering. 2024;57(1),429-449.

[9] DAI XL, GAO R, DU F, et al. Evolution and control of overburden fracture in extra-thick coal seam mining with hard roofs: ground grouting sealing and case study. Bulletin of Engineering Geology and the Environment. 2024;83(7), 257-271.

[10] CHONG J, LAI XP, CUI F et al. Mining pressure distribution law and disaster prevention of isolated island working face under the condition of hard "umbrella arch". Rock Mechanics and Rock Engineering. 2024;57(10),8323-8341.

[11] XU HX, ZHANG Q, WANG K, et al. Analytical solutions for the deflection and internal force of a hard roof subjected to a piecewise linear supercharged load. International Journal of Geomechanics. 2024;24(7),135-152.
[12] BO HZ, GUO GL, LI HZ, et al. Study on surface subsidence prediction method of shallow coal seam backfill-strip mining under the hard roof. Bulletin of Engineering Geology and the Environment. 2023;82(7), 106-132.
[13] HUANG BX, HOU MX, ZHAO XL, et al. Experimental investigation on the reformation and strength weakening of hard limestone by acidizing. International Journal of Mining Science and Technology. 2022;32(5), 965-979.
[14] ZHANG FT, WANG XY, BAI JB, et al. Study on hydraulic fracture propagation in hard roof under abutment pressure. Rock Mechanics and Rock Engineering. 2022;55(10),6321-6338.
[15] WEI C, YU LY, ZHANG B, et al. Study on mechanisms of hydraulic fracture propagation under pre-pulse combined hydraulic fracturing. Journal of Mining and Safty Engineering. 2025;42(06),54-61.
[16] TENG T, LIANG X, XU Z,et al. Interlayer effect and evolution law of hydraulic fracture propagation in composite layered rocks. Journal of Mining and Strata Control Engineering. 2025,12(07), 103-114.
[17] YANG Z, SHI XM, WANG YL, et al. Optimized design of narrow coal pillars under hard roof and inclined seam conditions based on fracture behavior and stability analysis. Bulletin of Engineering Geology and the Environment. 2025;84(11),484.
[18] LI HL, LIU HuD, LIU CY, et al.Phase field model and numerical simulation study of hydraulic fractures for roadway roof pressure relief. Journal of China University of Mining and Technology.2025;54(5),971-983.
[19] YAN JW, LIANG WG, SONG XX. Distribution of quartz sand and coal fine in coal seams after hydraulic fracturing and its impact on coalbed methane extraction. Journal of China Coal Society. 2025;32(11),206-218.
[20] MA JQ, WANG HS, DONG GW, et al. Hydraulic fracture propagation path and intelligent prediction of fracturing effects in coal measure strata. Journal of Mining and Strata Control Engineering.2025; 7(6), 063029.
[21] FANG XJ，WU CF，SHEN J，et al. Transformation effect and energy control mechanism of hydraulic fracturing in deep coal reservoirs. Journal of China University of Mining & Technology. 2026; 55(01), 193-212.
[22] LI QG，ZHAO YL，HU QT，et al. Denoising method and application of microseismic signals for coal seam hydraulic fracturing based on deep neural network mode. Journal of China Coal Society, 2025; 50(8),3916−3932.
[23] HUANG BX, XING YK, LI BH, et al. Discussion and prospects on induced seismicity from shale gas extraction: A case study of the Sichuan Basin. International Journal of Rock Mechanics and Engineering. 2025;44(11), 236-248.
[24] HUA H, CHENG BJ, XU TJ, et al. Distributed optical fiber acoustic sensing-based optimization of microseismic source localization in the hydraulic fracturing for coalbed methane production. Coal Geology and Exploration. 2025; 53(02), 326-341.
[25] TAN Y, WANG Y, HE MC, et al. Multi dimensional segmented hydraulic fracturing impact ground pressure control and loss reduction technology for deep buried thick coal seam hard roof. Journal of China Coal Society. 2025; 50(2), 794−809.
[26] SUN YT, BI RY, SUN JB, et al. Stability of roadway along hard roof goaf by stress relief technique in deep mines: a theoretical, numerical and field study. Geomechanics and Geophysics for Geo-Energy and Geo-Resources. 2022; 8(2),236-251.
[27] HAN CL, YANG HQ, ZHANG N, et al. Study on reasonable coal pillar width of gob-side roadway excavating with multi-layer hard roof in western deep mine. Geotechnical and Geological Engineering. 2021;40(03),1-12.
[28] TANG W, ZHAI C, XU JZ, et al. The influence of borehole arrangement of soundless cracking demolition agents (SCDAs) on weakening the hard rock. International Journal of Mining Science and Technology. 2021;31(2),197-207.
[29] ZHAO TX, ZHANG PF, ZHANG XF, et al. Microseismic behavior during mining of the working face under blasting presplitting of a hard roof. International Journal of Geomechanics. 2024;24(3),169-184.
[30] LI TC, FAN LJ, ZHU QW, et al. Research on the impact and control techniques of gangue rib in hard roof. Engineering Failure Analysis. 2024;157,107899.
[31] XIA BW, MA ZK, ZHOU L, et al. Decoding the hard roof control mechanism of ground fracturing based on the material point method. Rock Mechanics and Rock Engineering. 2025;58(8),1-16.
[32] YAN H, MAO WH, ZHANG JX, et al. Experimental investigation into the propagation law of supercritical carbon dioxide fracturing cracks induced by directional grooving of hard roof. Rock Mechanics and Rock Engineering. 2024;57(12),1-15.
[33] Hou MX, Huang BX, Zhao XL, et al. Influencing factors analysis of hard limestone reformation and strength weakening under acidic effect. Journal of Central South University. 2024;31(7),2446-2466.
[34] ZHANG HR, LIU CY, LIU HD, et al.Study on asymmetric floor heave mechanism and hydraulic fracturing control of mining-affected roadway. Journal of Mining and Safty Engineering. 2026;43(02),265-279.
[35] LIU JW, LIU YY, LIU CY, et al.Controllable vertical cutting method for double-layer hard roofs in mining faces using hydraulic fracturing. Journal of Mining and Safty Engineering. 2025;42(06),369-381.
[36] LIN YK, LIU JW, CHEN SJ, et al. Experimental study on fractures propagation law and fractures mechanism of gel fracturing. Coal Science and Technology. 2025;53(11), 284−294.
[37] WANG HY, LU C, SU X, et al. Influence mechanisms of cleats on hydraulic fracture propagation in deep coalbed methane reservoirs. Coal Geology and Exploration.2026;54(2),103−114.
[38] SHI Y, WANG ZL, CHENG LX, et al. Application and effectiveness evaluation of hydraulic fracturing for roadway pressure relief in coal mines. Chinese Journal of Rock Mechanics and Engineering. 2025;44(02),206-224.

[39] ZHANG HW，ZHOU CH，HE J，et al. A coupled simulation method of hydraulic fracturing for relieving mining pressure under hard roof based on DEM method. Journal of China Coal Society.2025; 50(S1),39−49.
[40] MA JQ, LI XH, ZHANG JQ, et al. The study on the propagation laws of hydraulic fractures in coal measure strata under true triaxial conditions. Journal of Mining and Strata Control Engineering. 2025; 7(04), 043027.
[41] ZOU WK, LI GQ, ZHANG JH, et al. Prediction of permeability and fracture pressure of underlying pressure-relieved coal-bearing strata in goaf of Sihe Mine. Journal of China Coal Society.2025;50(S1),437−448.
[42] ZHANG YJ, XU ZY, LI S, et al. Key technology and application of ultra-high pressure water jet “cutting-pressure joint” pressure relief and permeability enhancement. Coal Science and Technology. 2025; 53(09),201−212.
[43] MA D, YAN JH, HOU WT, et al. Method and technology for efficient hard rock breaking through fracturing modification and enhanced cuttability. Journal of Mining and Safety Engineering. 2025;42(04),256-274.
[44] ZHAO ZH, DENG YZ, GUO JC, et al. Evolution law and field application of true triaxial fracture of deep coal rockunder different injection modes. Chinese Journal of Rock Mechnics and Engineering. 2025;44(10),367-392.
[45] SHEN LF, HUA T, WANG ZL, et al. Effect of parameter spatial variability on fracture propagation morphology of rock hydraulic fracturing. Rock and Soil Mechanics. 2025;46(04),249-267.
[46] LI J, LIU Pl LI NY. Physical simulation study on the transport of biomimetics dandelion proppant in similar coalbed methane fracture network. Journal of China Coal Society. 2025; 50(2), 1148-1161.
[47] DU TT, JU WJ, LU ZG, et al. Experimental study on mechanical properties of rock degraded by hydraulic fracturing. Coal Science and Technology.2025;53(10),74−83.